Soft Matter

PAPER

View Article Online
View Journal | View Issue

Cite this: *Soft Matter*, 2018, **14**, 7264

Structure, rheology, and microrheology of wormlike micelles made of PB–PEO diblock copolymers†

Antonio Tavera-Vázquez, [a] Brisa Arenas-Gómez, [bc] Cristina Garza, [a] Yun Liu [cd] and Rolando Castillo *[a]

A diblock copolymer made of poly(1,4-butadiene)-*block*-polyethylene oxide, with a degree of polymerization of the polybutadiene and polyethylene oxide blocks of 37 and 57, respectively, self-assembles in water as worm-like micelles determined by small angle neutron scattering with an average diameter of ∼12.7 nm, a core radius of ∼2.7 nm, a shell radius of ∼3 nm, and an estimated persistence length of >225 nm. Worm-like micelles of almost the same diblock copolymer, but with a smaller polyethylene oxide block (degree of polymerization 45) were also measured. The worm-like micelles were also observed with negative staining using low energy electron microscopy. The boundary between dilute and semidilute regimes was estimated to be ∼0.8 wt%. The viscoelastic spectra at low and intermediate frequencies do not follow the Maxwell model. These micelles do not present the same rheological behavior of worm-like micelle solutions of conventional surfactants. The slow dynamics of the self-assembly explains this uncommon behavior for the system. Any micellar rearrangement is impeded due to the extremely high hydrophobicity of the polybutadiene block; stress mainly relaxes by the reptation mechanism. Using diffusive wave spectroscopy, we measured the mean square displacement of particles in the micellar solution. From the mean square displacement, we obtained $G'(\omega)$ and $G''(\omega)$ at high frequencies. $|G^*|$ exhibits a power law behavior showing the stress relaxation changes as frequency increases, first dominated by the Rouse–Zimm modes and then by the bending modes of the Kuhn segments. This allowed us to estimate the worm-like micelle persistence lengths that depend on the copolymer concentration.

Received 26th July 2018,
Accepted 9th August 2018

DOI: 10.1039/c8sm01530a

rsc.li/soft-matter-journal

1. Introduction

The self-assembly of small amphiphiles has been studied since a long time, and various morphologies have been observed in aqueous solutions, for example micelles, cylindrical micelles, bicontinuous structures, lamellae, vesicles, *etc.*[1,2] The packing of the amphiphile molecules mainly determines the morphology of these supramolecular structures that are also found in the self-assembly of diblock copolymers (DBCPs).[3] However, compared to small-molecule aggregates polymer aggregates exhibit a higher stability, attracting considerable attention because of their potential applications in many fields, such as biomedicine, biomaterials, microelectronics, photoelectric materials, catalysts, *etc.*[4–7]

DBCPs form aggregates in solution whose morphology can be tuned by varying the chemical nature of the blocks, as in the case when a block is solvophilic and the other blocks are solvophobic, their molecular weight, or their ratio. The preferred morphology will be fixed by the spontaneous curvature of the assembly which is determined by the most efficient packing of the involved aggregates.[1,2] The spontaneous curvature optimizes the system energetically. However, it does not account for the effects of entropy that also can stabilize some structures and defects. Below the critical micelle concentration (CMC) which is quite low in diblock copolymers, entropy favors a uniform dissolution of the amphiphile in the solvent; aggregation is negligible. Above the CMC, interaction dominates and entropy effects are reduced. Consequently, the number of aggregates usually of a spherical form sharply increases. Subsequently, cylindrical micelles are formed when amphiphilic DBCPs have a moderate spontaneous curvature, lower than spherical

[a] *Instituto de Física, Universidad Nacional Autónoma de México, P.O. Box 20-364, 01000, México City, Mexico. E-mail: rolandoc@fisica.unam.mx*
[b] *División de Ciencias e Ingenierías, Campus León, Universidad de Guanajuato, Loma del Bosque 103, Lomas del Campestre, 37150 León, Guanajuato, Mexico*
[c] *Center for Neutron Research, National Institute of Standards and Technology, Gaithersburg, MD, 20899, USA*
[d] *Department of Chemical and Biomolecular Engineering, University of Delaware, Newark, DE, 19716, USA*

† Electronic supplementary information (ESI) available. See DOI: 10.1039/c8sm01530a

micelles but larger than vesicles or bilayers. Here, energy is optimized when the curvature is uniform everywhere, forming extended linear structures usually named worm-like micelles (WLMs). Nevertheless, entropy introduces in the system a degree of randomness through bending of cylindrical micelles, which adds conformational entropy like the configurational entropy of polymeric chains, and through topological defects, in the form of end-caps and branch junction points. When these two defects appear, regions with different local curvatures are formed but incur different energetic penalties. The overall entropic gain associated with end-caps is higher than that of branch points. Although the appearance of topological defects introduces an entropy gain, the type of defects that dominate is set by the amphiphile spontaneous curvature. If the scission energy of a WLM (the energy required for creating two end-caps from an infinite cylinder) is large enough, then the semi-flexible linear micelles may become very long and entangled. End-caps increase entropy by increasing the number of micelles in the system. Thus, lowering the scission energy shortens the total contour length of the linear micelles. On the other hand, branch junction points increase the number of possible configurations, enabling percolation and the formation of extended micellar networks, which lead to a multi-connected rather than an entangled network of cylindrical micelles. A review about junction and end-cap formation can be found elsewhere.[8] The complex interplay between the molecular geometry and the amphiphilic characteristic of both blocks determines the organization of supramolecular structures, although the solvent composition plays an important role,[9,10] because of the free energy contribution from the interfacial tension between the solvent and the insoluble block.

One of the most extensively studied DBCP types forming WLMs is the polybutadiene–polyethylene oxide (P(1,2)B–PEO) rich in 1,2-microstructure (IUPAC name: poly-1-vinylethylene);[11–16] see Fig. 1. The morphology of the supramolecular structures of these copolymers depends on the weight fraction (w_{PEO}) of the hydrophilic polyethylene oxide (PEO) and the degree of polymerization of the hydrophobic block, P(1,2)B. Even though the full phase diagram of these systems is not known, the weight fraction where different structures (micelles, WLMs, lamellas, *etc.*) are located is approximately known.[13,17] P(1,2)B–PEO forms WLMs in aqueous solutions at a concentration of less than 5 wt%. One important difference between small non-ionic surfactants and PBPEO copolymers dispersed in a polar solvent, such as water, is the value of the CMC. For the former, the CMC is not too low; molecular exchange and equilibration are relatively rapid. In contrast for the latter, the CMC is very small ($\leq 10^{-6}$ mol L^{-1}) and decreases as temperature increases. The molecular exchange is extremely slow, and the presence of free chains in solution is practically negligible. This impediment of micellar rearrangement has its origin on the extremely high hydrophobicity of the P(1,2)B block; therefore, aggregates in water are not necessarily in equilibrium. For WLMs of P(1,2)B–PEO, no exchange of unimers between aggregates through the solvent has been detected[18] and equilibrium is never achieved.[14] This failure to globally equilibrate has consequences in the distribution of morphologies and polydispersity and the particles are kinetically trapped in these dispersions. These effects are evident even at molecular weights of just 2000 Da. There are just a few reports on the rheological properties of P(1,2)B–PEO in water solution, particularly when they self-assemble in WLMs.[12,19,20]

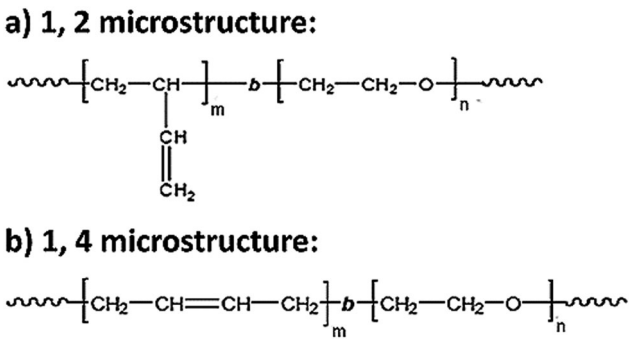

Fig. 1 Diblock copolymers of the type polybutadiene–polyethylene oxide showing two different polybutadiene microstructures: (a) P(1,2)B; source name: 1,2-poly(1,3-butadiene); IUPAC name: poly 1-vinylethylene. (b) P(1,4)B; source name: 1,4 poly(1,3-butadiene); IUPAC name: poly(but-2-ene-1,4-diyl). At the very end, both terminal groups end with hydrogen.

The DBCPs of the type PBPEO in water solution rich in 1,4-microstructure (Fig. 1) are even less studied. They also self-assemble in spheres, cylinders, or bilayers when the polymer blocks have a degree of polymerization m = 46, and n = 35, 39, 42, 44, and 56.[14] Recently, our group has reported the structure and rheological behavior of WLMs made of PBPEO rich in 1,4 microstructure (1,4 poly(1,3-butadiene)–polyethylene oxide diblock copolymer) in water, where the degree of polymerization of the PB and PEO blocks was 37 and 45, respectively.[21] This system will be called from now on PBPEO45, and its concentration in water is limited to be $\leq$2.5 wt% to avoid phase separation. Small X-ray scattering (SAXS) revealed that the PBPEO45 self-assembles in worm-like micelles with a diameter of $\sim$12 nm. However, this system does not follow the rheological behavior of worm-like micelle solutions made of conventional surfactants. The viscoelastic spectra did not follow the Maxwell model at low and intermediate frequencies. The slow dynamics of the self-assembly explains this uncommon behavior for this worm-like micellar system due to the extremely high hydrophobicity of the PB block that does not allow any micellar exchange rearrangement through water; the system is dynamically arrested.

The purpose of this report is to present: [1] the rheology and microrheology of water solutions embedded with self-assembly aggregates of a PBPEO diblock copolymer where the PB block is rich in 1,4-microstructure (Fig. 1), and with the same degree of polymerization of the PB block in the PBPEO45, but with the PEO block larger, *i.e.*, with a degree of polymerization n = 57, this will be called PBPEO57, as seen below, this system also self-assembles in WLMs; [2] the microrheology of the micellar solution of PBPEO45; and [3] a comparison for the first time of the rheological behavior at a high frequency of both micellar solutions with those of conventional surfactants.

The rheology of the aqueous solution of PBPEO57 in water will be determined, *i.e.*, flow curves and the viscoelastic spectra

at different polymer concentrations. The concentration of PBPEO57 ($C_{PBPEO57}$ in wt%) is limited in this study to $C_{PBPEO57} \leq 9$ wt% to avoid phase separation. The mean square displacement (MSD) of particles embedded in the micellar solutions under study will be determined using diffusive wave spectroscopy (DWS). From the MSD, the high-frequency complex modulus $G^*(\omega)$ is obtained. The questions that we would like to answer in this study are: can we obtain structural information about the systems of interest here from the microrheology results? Moreover, is the stress relaxation observed by the rheology and microrheology notably modified when PEO size is increased? Before making these measurements, there is a need to determine the morphology of the self-assembled structures in the PBPEO57 solution. We use small angle neutron scattering (SANS), and we observe them with negative staining using a low energy transmission electron microscope and a scanning microscope. To complete this report, we included the SANS scattering for the PBPEO45 micellar solution.

2. Experimental section

2.1 Materials

Poly(but-2-ene-1,4-diyl)-*block*-poly(oxyethylene) block copolymers (–[CH_2–CH═CH–CH_2]$_m$-*b*-[CH_2CH_2–O]$_n$–) PBPEO57 and PBPEO45 were purchased from Polymer Source (Canada); they were used as received. Data given by the manufacturer for PBPEO57: m = 37, n = 57, M_w = 4500 g mol^{-1}, 2000-*b*-2500, PB block rich in 1,4 microstructure >85, M_w/M_n = 1.08, *trans*/*cis* ratio ~ 40/60. For PBPEO45: m = 37, n = 45, M_w = 4000 g mol^{-1}, 2000-*b*-2000, PB block rich in 1,4 microstructure >93 wt%, M_w/M_n = 1.08, *trans*/*cis* ratio ~27/68, and 1,2 microstructure ~5 wt%. Water was deionized (Nanopure-UV, USA; resistivity ~ 18.3 MΩ cm). 2 μm tracer microspheres for DWS experiments are made of plain polystyrene (Bangs Laboratories, Inc.); they are negatively charged in pure water due to the negatively-charged sulfate groups that populate the surface of the plain polystyrene beads.

2.2 SANS

SANS measurements were performed on the NG7 SANS beamline at the Center for Neutron Research at the National Institute of Standards and Technology (Gaithersburg, MD). A broad scattering vector range was set at various neutron wavelengths with three sample-detector distances: 1 m, 4 m and 13 m with eight, four, and one beam guides, respectively; $\Delta\lambda/\lambda$ = 0.12, where λ is the neutron wavelength. The samples were measured in titanium cells (2 mm path length with quartz windows) at a constant temperature of 20 °C. The scattering data were averaged over 2000 s. Raw data were reduced and analyzed using the Igor Pro SANS software according to standard methods.[22] Finally, all data were corrected for detector response characteristics before their analysis.

2.3 Rheology measurements

Rheological measurements were carried out using a MCR 702-TwinDrive rheometer (Anton Paar, Austria). Flow curves and oscillatory measurements were performed using a cone-plate geometry (2°; diameter, 40 mm) with temperature control. Solutions were allowed to relax at rest for two days before the measurements.

2.4 Microrheology with diffusive wave spectroscopy (DWS)

The viscoelastic spectrum can be extended to high frequencies that cannot be reached using mechanical rheometers. In microrheology, the MSD, $\langle \Delta r^2(t) \rangle$, of particles embedded in a complex fluid is measured by DWS, and the measurement can be related to $G^*(\omega)$ using a generalized Stokes–Einstein equation:[23]

$$G^*(\omega) = G'(\omega) + iG''(\omega) = \frac{k_B T}{\pi a i\omega \Im(\langle \Delta r^2(t) \rangle)(\omega)}. \quad (1)$$

where $\Im$ is the unilateral Fourier transform, a is the particle diameter, ω is the frequency (angular), k_B is the Boltzmann's constant, and T is the temperature. Our DWS setup is a home-made instrument described elsewhere.[24] Typical acquiring times are around 600 s to 900 s, enough sampling time due to the fast relaxation of the systems under study.

In the DWS theory, the $\langle \Delta r^2(t) \rangle$ of probe particles can be determined by collecting their scattered intensity over a sufficiently long collection period and evaluating the time-averaged intensity auto-correlation function (ACF), $g^{(2)}(\tau)$. This function can be calculated for a plane wave passing through a sample, with the scattering particles immersed in it, in a slab-shaped container of thickness $L \gg l^*$, and infinite transverse extent.[24] Here, l^* is the mean free path of light that can be obtained from transmittance and reflectance measurements of the investigated samples using an integrating sphere.

Some diblock copolymer suspensions present an additional complication because DWS assumes that the system under study is entirely transparent to the incident light beam. Nevertheless, the PBPEO45 and PBPEO57 systems are turbid even at very low concentrations, to overcome this inconvenience, experiments were performed using the inverse adding-doubling method (IAD),[25,26] which allows us to calculate the optical parameters of the sample, with and without particle tracers: the transport mean free path, l^*, the absorption length, l_a, and the anisotropy coefficient, g. The comparison of the calculated parameters with and without tracers allows us to estimate the contribution to the scattered light of the pure diblock copolymer system. The estimation of l_a allows us to use a correction to the DWS correlation function, and hence to the MSD of the tracers for the first time in a turbid complex fluid, using the method developed by Sarmiento-Gomez *et al.*[27] Knowing the numerical values of l^* and l_a, and measuring the intensity autocorrelation functions, $g^{(2)}(\tau)$; the MSD of the microspheres can be obtained when there is light absorption in the fluid of interest that cannot be neglected.

The experimental MSD curve is fitted to a model curve proposed by Bellour *et al.*,[28] which predicts an expected behavior of the particles when they are immersed in a typical WLM solution over several decades in time. Finally, each of the components of $G^*(\omega)$ is obtained using the fitted Bellour model curve in eqn (1).[29] In a few tests using 0.8 μm microspheres, we confirmed that the size particle does not affect the results.[28]

2.5 IAD method

This is a method developed for optical parameters recovery.[25,26] It starts with three measurements for each sample: total reflectance of light, total transmittance of light, and collimated transmittance of light. These measurements serve as comparison parameters with those estimated by the equation of radiative transport of light used in the IAD method. The optical output parameters of the inverted radiative transport equation are l^*, l_a, and g. Several steps are iteratively followed until a match with the experimental measurements is reached: (1) an educated guess for a set of optical parameters is given. (2) The reflectance and transmittance of the samples are predicted using the adding-doubling method. (3) Transmittance and reflectance are compared with the measured values. (4) If the match is not good enough, the set of optical parameters is modified using a minimization algorithm. IAD also considers several features experimentally difficult to assess, such as light lost out of the edges and nonlinear effects in the integrating sphere measurements.

2.6 Scanning electron microscopy (SEM)

Better surface information of specimens can be obtained when SEM is run at low accelerating voltages due to a more significant surface sensitivity and less beam damage, mainly because charging effects are reduced or even eliminated. We used an extreme-resolution analytical field-emission scanning electron microscope (SEM; JSM-7800F JEOL Ltd Japan) working at low electron acceleration voltages[30] on negatively stained samples of the systems under study. Low energy STEM (Scanned Transmission Electron Microscopy)-in-SEM was also employed in addition to the backscattered electrons to survey the samples. This is a powerful technique that permits imaging soft material samples with lower accelerating voltages (less than 30 kV) and larger fields of view.

2.7 Sample preparation

SEM. Standard TEM grids covered first with a collodion layer and then covered with a layer of carbon were used to deposit the specimens of the systems under study. The grid is placed over a piece of filter paper, and a few microliter drop of the diblock copolymer solution is deposited on it ($\sim$5 μl). After 2 or 3 min, a drop of phosphotungstic acid (3 wt%) is subsequently added to the sample. The filter paper absorbs the excess of deposits on the grid, and the sample is dried under ambient conditions. Before placing it on the microscope, the sample was covered with a thin carbon layer to ensure that the sample on the grid is conductive.

Rheology. PBPEO stock water solutions were prepared by weight and stirred for 14 days at 40 °C before use. No phase separation was observed up to $C_{PBPEO57}$ = 9.0 wt% and up to $C_{PBPEO45}$ = 2.5 wt%. Above these limits, phase coexistence appeared with one birefringent phase at rest, presumably a lamellar phase.

DWS. Solutions with a polymer concentration slightly above the desired concentration to be measured were prepared. Then, 2 μm microspheres (Bang Labs Inc.) in water suspension (10.17 wt%) were added while the samples were stirred; the particle volume fraction was 0.03. Stirring was maintained for 20 min to ensure a homogeneous dispersion. Sample sonication must be avoided to prevent breaking of the polymer chains. Samples were allowed to relax and thermalize at 20 °C in rectangular cuvettes of a light path thickness of 2.5 mm, for 10 min, because the samples have low viscosity and they are prone to particle sedimentation.

3. Results and discussion

3.1 Structure of the aggregates

Determining the aggregate structure in a system is critical for understanding its rheological behavior. Therefore, in this section, we describe our results using SANS and SEM.

SANS. We measured the static SANS pattern for the diblock copolymer micellar solution made of PBPEO57 at 0.5 wt%, dissolved in deuterated water in the dilute regime. It is presented in Fig. 2a as a function of q ($\boldsymbol{q}$ = scattering vector); for comparison, we also included the measurements for the WLM system made of PBPEO45. The scattering curves cover q values from 0.0008 to 0.2 Å^{-1} which correspond to length scales of $2\pi/q \sim$ 20–6000 Å corresponding to systems made of small structures. In Fig. 2a, the scattering patterns display a $\sim q^{-1}$ dependence at low q values, although a slight deviation between the scattering functions for both diblock copolymers can be observed; meanwhile, at intermediate and high q there is no significant difference. These patterns are typical of extended cylindrical structures, as previously observed with SAXS in the case of the PBPEO45 that self-assembles in a core–shell cylinder.[21] Consequently, the mean radius for both tubular structures is quite similar. The scattering window for flexible cylindrical structures usually includes the analysis of three different regions: at low q and at intermediate q in the Guinier regions, and at high q in the Porod region.[31–33] Here, the low q Guinier region is not accessible with the present instrument configuration. At high q (Porod region), the scattering arises from the local cross section of the rodlike aggregates and the scattering patterns commonly present oscillations.

Cross-sectional size. For cylinders at intermediate q, the scattering function can be described by $I(q)q = K\chi \exp(-q^2 R_{g\text{-}cs}{}^2/2)$ where χ is a constant related to the size of the cylindrical aggregates, and $R_{g\text{-}cs}$ is the cross-sectional radius of gyration. The contrast factor K is given by $K = (b_m - V_m\rho_s)^2$, where b_m is the sum of neutron scattering lengths, V_m is the volume per surfactant monomer in the micelle, and ρ_s is the scattering length density of the solvent.[31,32] When the cross-section is circular, the cylinder radius is $R_{CS} = \sqrt{2}R_{g\text{-}cs}$.[31,32] Intermediate Guinier fits of our diblock copolymer systems are shown in Fig. 2b. The linearity of data indicates the extended cylindrical nature of the micelles. The fitting reveals a total cross-sectional diameter of 12.70 nm and 12.77 nm for PBPEO57 and PBPEO45, respectively; see Table 1. There is no significant difference between the cross-section of both diblock copolymer WLMs. The diameter of the PBPEO45 WLMs is similar to the previous value obtained using SAXS ($\sim$12.4 nm).[21]

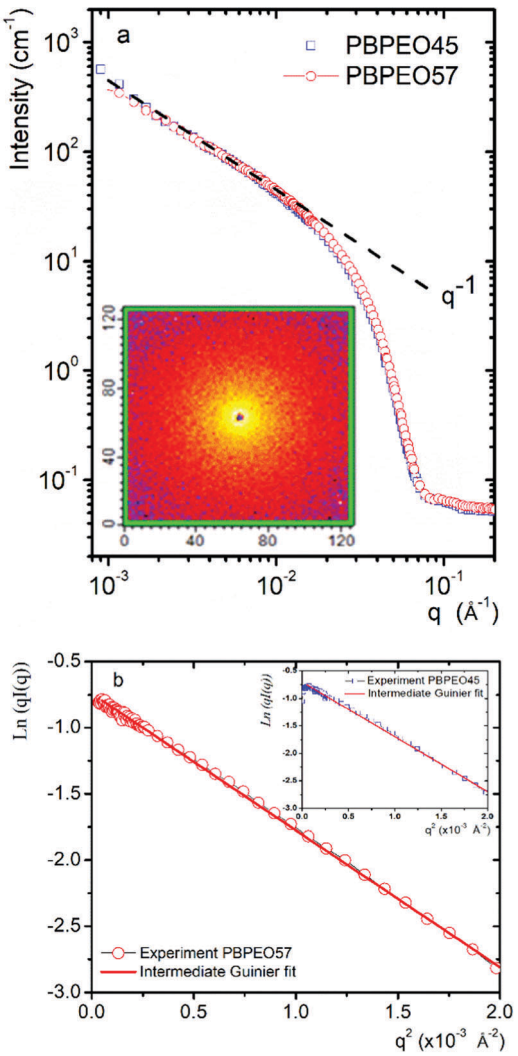

Fig. 2 (a) Static SANS patterns for both diblock copolymers PBPEO57 and PBPEO45 dissolved in deuterated water at 0.5 wt%. Open symbols represent experimental data and the dashed line is a guide to the eye. Inset: The 2D-SANS scattering pattern of PBPEO57. (b) Intermediate Guinier plots for PBPEO57 (main figure) and PBPEO45 (inset).

Core–shell structure. A core–shell cylinder model is used to fit the data for both copolymer systems to extract useful information from the intermediate and large q regions; best fits are obtained when polydispersity in the core radius is included.[34] Therefore, the resulting scattering of each particle is the scattering intensity with a specific size weighted by the polydispersity of a cylinder core, modeled with a normalized log-normal distribution. The fitting to the SANS patterns are presented in Fig. 3a and b, and the calculated model parameters are in Table 1. The overall intensity of the core–shell model is given by:

$$I(q) = \text{background} + \frac{\text{scale}}{V_p}\sum_{R_p} n(R_p, \sigma_p) P\left(q, R_p, R_l, H_p, H_l, \rho_p, \rho_l, \rho_{solv}\right)$$

where the normalized log-normal function is given by:

$$n(R_p) = \frac{\exp\left(-\frac{1}{2}\left[\frac{\ln(R_p/R_o)}{\sigma_p}\right]^2\right)}{\sqrt{2\pi}\sigma_p R_p}$$

and

$$P(q) = \int_0^{\pi/2} \sin\theta \cdot d\theta \left[V_l(\rho_l - \rho_{solv}) \frac{\sin\left(\frac{qH_l\cos\theta}{2}\right)}{\frac{qH_l\cos\theta}{2}} \frac{2J_1(qR_l\sin\theta)}{qR_l\sin\theta} + V_p(\rho_p - \rho_l) \frac{\sin\left(\frac{qH_p\cos\theta}{2}\right)}{\frac{qH_p\cos\theta}{2}} \frac{2J_1(qR_p\sin\theta)}{qR_p\sin\theta} \right]^2.$$

Here, $J_1(x)$ is the first order Bessel function, θ is the angle between the cylinder axis and $\boldsymbol{q}$. V_i and ρ_i refer to volumes and densities, where the subscripts i = p, l and solv represents parameters for core, corona and solvent, respectively. H_l is the full cylinder contour length, R_l is the full cylinder radius, H_p is the core contour length, R_p is the core radius, and R_o is the mean core radius. These variables incorporate the dimension of the bare particle, taking into account the radial thickness (R_l = R_p + radial thickness) and the face thickness, x, given by $2x = H_l - H_p$. σ_p is the standard deviation of the log-normal distribution. Upon setting the scattering length density of D_2O (ρ_{D_2O} = 6.4 × 10^{10} cm^{-2}) and a relatively large polydispersity (σ_p/mean size value = 0.28) the fits show a good agreement with the SANS data (Fig. 3a and b), although the fitting is not so good at low q, because this model does not consider cylinder flexibility. The contour length is outside the experimental resolution ($L_C \gg 1/q_{min}$) and it was set at ~1 μm. The data show a poor contrast at high q compared with SAXS.[21] For both systems, L_C seems to be larger than 600 nm; therefore, the aggregates are WLMs. The total diameter obtained from this fitting model differs from that deduced from the linear decrease in the intermediate Guinier fits (see Table 1).

Table 1 WLM parameters obtained with the different fitting models and errors between experimental data and models

	Model				
	Intermediate Guinier	Polydisperse core–shell cylinder			Polydisperse radius flexible cylinder
	Diameter (nm)	Diameter (nm)	Mean core radius (nm)	Shell thickness (nm)	Persistence length (nm)
PBPEO57	12.70 ± 0.01	11.42 ± 0.08	2.69 ± 0.01	3.02 ± 0.03	>225
PBPEO45	12.77 ± 0.02	11.52 ± 0.1	2.64 ± 0.02	3.12 ± 0.03	141

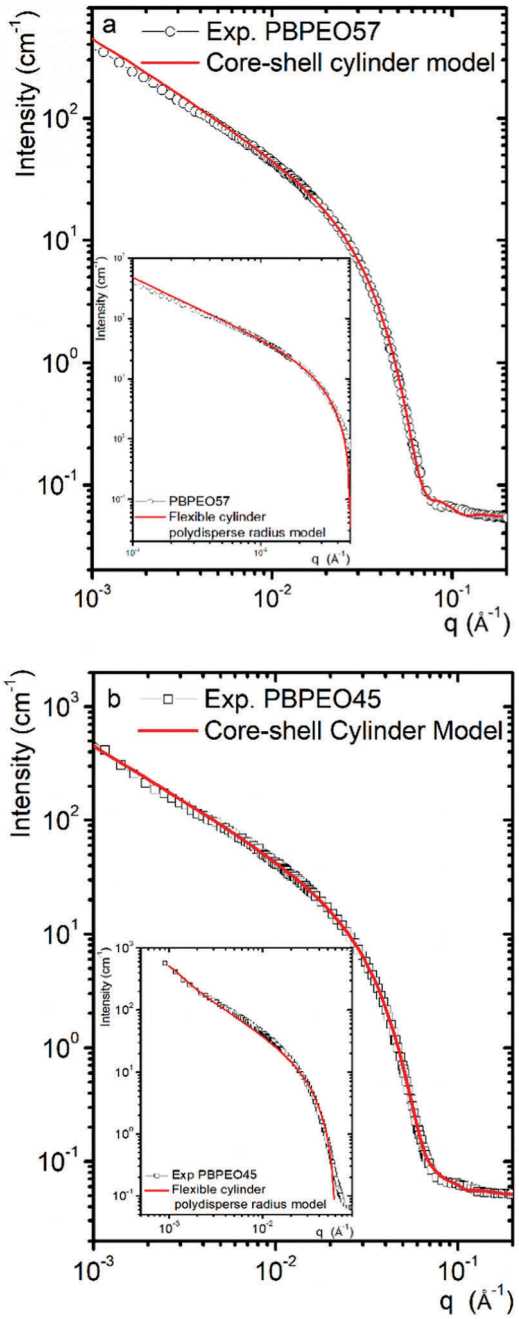

Fig. 3 Scattering curves and fitting models. A core–shell cylinder model with polydispersity in the core radius: scattering curves for (a) PBPEO57 and (b) PBPEO45. Insets: Flexible cylinder model with polydispersity in the core radius. Open symbols: experimental data and lines: fittings.

WLM flexibility. At $q \sim 0.001$ Å^{-1}, we observe an inflection point for the PBPEO45 WLMs which is an indication of their flexibility. In contrast, PBPEO57 does not present any change in its slope. The contour length of flexible cylinders can be described as a chain of locally stiff segments of persistence length $l_p = b/2$; b is the Kuhn length. This suggests that the lengths of the stiff segments of PBPEO57 are larger than those of PBPEO45. In this low q region, we used a flexible cylinder model to fit the data to get some approximate value of l_p in these systems; see insets Fig. 3a and b and Table 1. For the fitting, the form factor for a flexible cylinder with a circular cross-section and a uniform scattering length density is used.[35,36] This model excludes volume interactions within the walk of a single cylinder. Intermicellar interactions are not included. Polydispersity is included using a Schulz distribution for the cross-section. To reduce the number of fitting parameters, we used R_{CS} (obtained from Guinier fit) and the scattering length density of D_2O. Our results indicate that WLMs of PBPEO45 are more loosely entangled than those of the PBPEO57 system. Only for the former, it was possible to estimate its persistence length ($l_p \sim 141$ nm). For the later, the flexibility effect cannot be seen in the scattering window, but it seems to be larger than 225 nm. Further studies achieving lower qs are needed to confirm these findings. A relation between the WLM hydrophobic core diameter d_c and l_p has been proposed for a series of PEO-based diblock copolymer amphiphiles,[37] which scales as $l_p \sim d_c^{2.8}$. The smallest hydrophobic block used in this case was P(1,2)B45–PEO55 which has a core diameter of 14.2 nm and a persistence length ~500 nm. In our case, l_p does not seem to follow this relation.

A comment can be done about the ideal form factors of monodisperse systems. It has been known for years that they do not represent real systems as well as expected.[46] Therefore, we expect differences in the parameters obtained with different models. In rod-like systems, we already know that the cross-section form factors produce strong oscillations at high q that have been observed in the WLMs of PBPEO45 with SAXS.[21] However, effects of low contrast, polydispersity, and instrument resolution can contribute to the smearing of the form factors; consequently, the smoothing of the real scattered intensity $I(q)$. In our SANS patterns, the oscillations are missing due to the low contrast and small diameter of the core–shell section. Introducing polydispersity in the core–shell model, we can improve the fitting to the experimental patterns. Notwithstanding the large polydispersity, the core and total radius obtained from the fitting seems to be acceptable.

Is it possible to explain the significant difference in l_p observed for the WLMs of both systems with almost identical core radius and shell thickness? Curiously, the WLMs with the larger PEO block (PBPEO57) present a shell thickness slightly smaller than in the other case. Necessarily, this block is more densely packed than in the case of PBPEO45. According to our SANS data, the hydrophilic PEO side chains are grafted to the hydrophobic PB polymer backbone as in cylindrical polymer brushes. The stiffness in this kind of polymer brushes is usually‘ explained through a balance between repulsive forces originating from steric overcrowding of the side chains and the entropic restoring force of the main chain preferring coiled configurations.[38] In PBPEO57, any bending will harshly increase the steric overcrowding because the PEO block is already more densely packed than PBPEO45. Consequently, the bending energy is more significant for the PBPEO57 WLMs than that for the PBPEO45.

Direct observation of the WLMs. Fig. 4 presents negatively stained micrographs of dilute samples made of PBPEO57

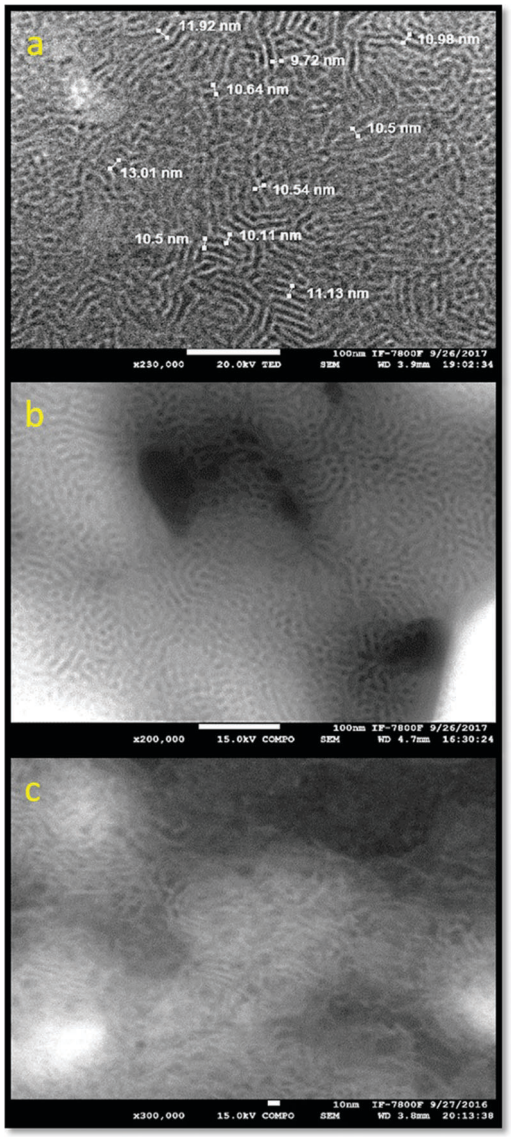

Fig. 4 Direct observation of WLMs made of PBPEO57 ($C_{PBPEO57}$ = 1.1 wt%): (a) STEM-in-SEM at 20 kV and (b) backscattered electrons at 15 kV, and for comparison (c) backscattered electron images for WLMs made of PBPEO45 at 15 kV ($C_{PBPEO45}$ = 0.6 wt%).

solutions obtained by SEM; we included an image for the PBPEO45 WLM solutions. In the low energy STEM-in-SEM image of dilute samples made with the PBPEO57 solution (Fig. 4a), a carpet of tubular structures is observed; no other kinds of structures are detected. We cannot estimate the total contour of the tubular structures, but we observe thread-like segments of a length of ~100 to 200 nm with an average diameter of ~11.4 nm. For the same system, Fig. 4b shows the same type of microstructure observed with backscattering electrons. For comparison, Fig. 4c presents an image also obtained with backscattered electrons for the PBPEO45 WLM solution that agrees with the tubular micellar structure obtained with SAXS experiments.[21] This image shows the same kind of microstructure of the PBPEO57 solution, but more

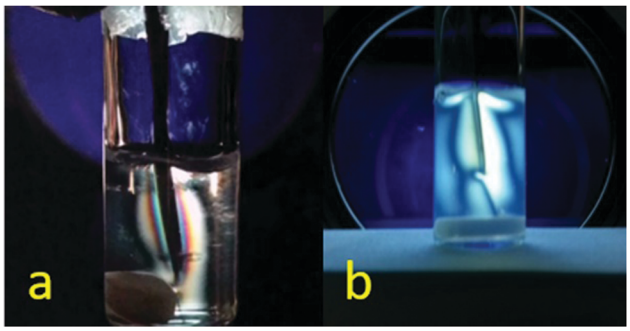

Fig. 5 Micellar solutions between cross polarizers under shearing when a spatula is slowly dipped into the fluid; (a) PBPEO57 at $C_{PBPEO57}$ = 5 wt%. (b) PBPEO45 at $C_{PBPEO45}$ = 2.5 wt%.

entangled. From these results, negative staining in conjunction with SEM and STEM-in-SEM is an easy and fast method to obtain the microstructure in this kind of micellar solutions, simpler than cryo-TEM.

At rest, dilute solutions of both diblock copolymers are not birefringent. However, as seen in Fig. 5, birefringence appears with shearing which is a typical behavior of WLM solutions that is typical when the system contains WLMs.

3.2 Mechanical rheology

Flow curves σ vs. $\dot{\gamma}$. Fig. 6a presents flow curves obtained by increasing the applied shear strain rate (logarithmic ramp) to the PBPEO57 micellar solutions, at different concentrations and T = 20 °C. These sweeps were performed approximately along five orders of magnitude in $\dot{\gamma}$. Shear stress increases in a nonlinear way (Fig. S1 in the ESI†). Although relatively concentrated PBPEO57 solutions present an important change of curvature in the σ *vs.* $\dot{\gamma}$ curves at $\dot{\gamma} \sim 1\ s^{-1}$, they do not present a clear plateau zone. For comparison, we included a flow curve for a micellar solution of PBPEO45 at $C_{PBPEO45}$ = 2 wt% which presents a clear plateau-like zone, which is typical of semidilute WLM solutions ($C > C^*$, overlap concentration). In contrast with conventional surfactants, before reaching the plateau-like region, in both cases, they do not present a shear thickening peak on the up-shear curve.

Viscosity. Fig. 6b presents the apparent viscosities $\eta(\dot{\gamma})$ for the PBPEO57 system determined with the measurements shown in Fig. 6a. The viscosity curves move upward as concentration increases. Viscosity values decrease several orders of magnitude and viscosity shear-thins as $\dot{\gamma}$ increases. At low concentrations ($C_{PBPEO57} \leq 3$ wt%), viscosity shear-thins in two steps. As determined using SANS, the system is made of WLMs; then once the system is sheared, the flow also tends to align the rod-shaped micelles along the fluid flow direction dropping the energy dissipation as in paranematic phases and as a consequence, viscosity decays dramatically. From the analysis of $\log\left[\lim_{\dot{\gamma}\to 0}\eta(\dot{\gamma})\right]$ *vs.* $C_{PBPEO57}$, a change of behavior is observed at ~0.8 wt% (not shown), that is $C_{PBPEO57}{}^*$ is ~0.8 wt%. This value is slightly larger than in the case of the micellar solution of PBPEO45 where $C_{PBPEO45}{}^*$ is ~ 0.6 wt%.[19] Below this

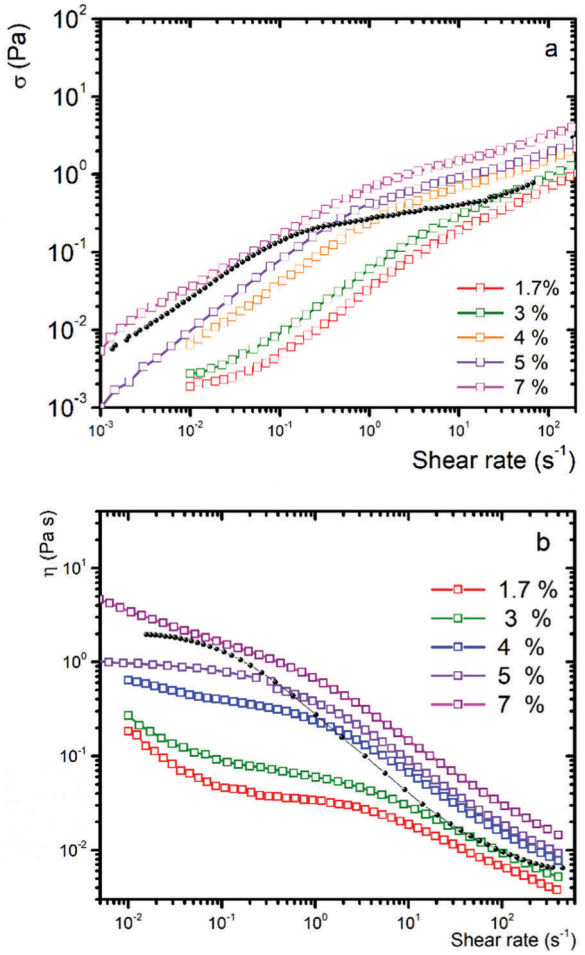

Fig. 6 (a) σ *vs.* $\dot{\gamma}$ curves for micellar solutions of PBPEO57 at different concentrations (open symbols). (b) Viscosity curves for micellar solutions of PBPEO57 at different concentrations (open symbols). For comparison, we also included in both figures the micellar solution of PBPEO45 at 2 wt% (full black symbols).

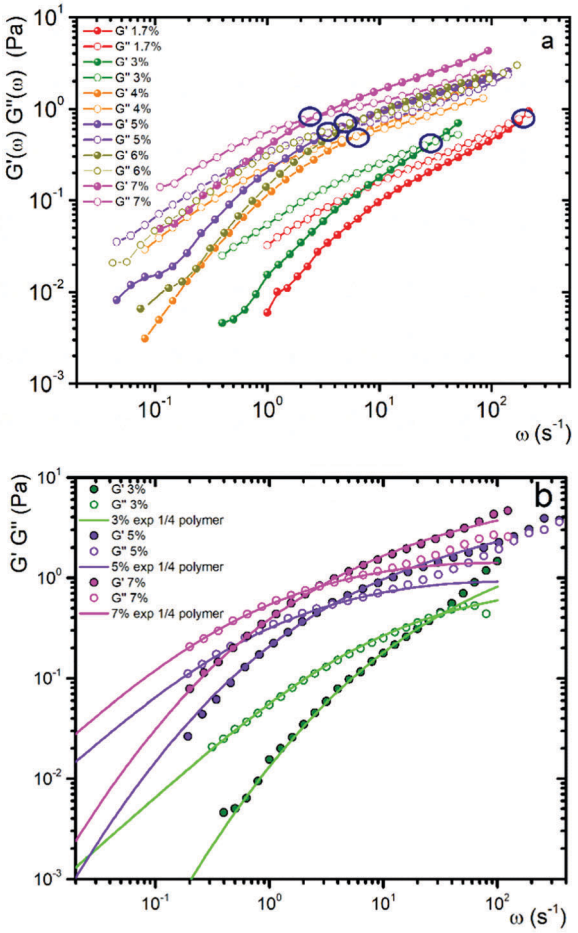

Fig. 7 (a) $G'(\omega)$ and $G''(\omega)$ as given by mechanical rheology for the PBPEO57 micellar solution. (b) $G^*(\omega)$ calculated with $G(t) \sim \exp(-(t/\tau_R)^{1/4})$ that corresponds to the case where polymer stress relaxes through reptation.

concentration, the interaction between micelles is apparently negligible, as in the dilute regime, where viscosity is low and relatively close to the solvent viscosity. Above this concentration, the micelles apparently start to entangle because viscosity increases drastically.

Viscoelastic spectra. In WLM solutions the shear modulus, $G(t)$, exhibits a time or frequency dependence. The latter is expressed through the complex modulus $G^*(\omega) = G'(\omega) + iG''(\omega)$; $G^*(\omega) = i\omega\int_0^\infty G(t)e^{-i\omega t}dt$. The real part of the complex modulus is the storage or elastic modulus in phase with the applied shear strain. The imaginary part is the viscous or loss modulus in phase with $\dot{\gamma}$.

Fig. 7a presents the viscoelastic spectra of the micellar solution for different $C_{PBPEO57}$, at low and intermediate frequencies (for comparison PBPEO45 is shown in Fig. S2 of the ESI†). In general, the solutions are more viscous at low frequencies, and at larger frequencies, after the crossing point between $G'(\omega)$ and $G''(\omega)$ curves, the solutions are more elastic. G_0, defined at the crossing point, (ω_0, G_0), is relatively constant between 0.4 and 0.7 Pa for all concentrations. This value is larger than for the micelles made of PBPEO45 ($\sim$0.18 Pa at $C_{PBPEO45}$ = 2.5 wt%) and other similar WLMs made of P(1,2)B–PEO ($\sim$0.25 Pa).[39] Our G_0 values are also lower than those for conventional surfactants where their G_0 is in the range of 1 to 1000 Pa. The crossover frequency, ω_0, decreases as the concentration increases. Inversely related, the relaxation time $\tau = \omega_0^{-1}$ increases as concentration increases. Fig. S3 of the ESI† presents a Cole–Cole plot of G''/G_0 *vs.* G'/G_0 for the solutions. As shown in this figure, there is no way for obtaining a semicircular fitting at low and intermediate frequencies at any concentration; this is a necessary condition for Maxwellian behavior usually followed by WLM solutions. Although this system forms WLMs as shown above, this unusual behavior could be explained because of the impediment of any micellar rearrangement, namely polymer exchange between micelles or breaking and recombination mechanisms, due to the extremely high hydrophobicity of the PB; the system is arrested. As previously reported, this behavior is also found in the PBPEO45.[21] Maxwellian behavior in WLMs is explained because local stress relaxes through a combination of reptation and breaking/recombination mechanisms;[40] the characteristic relaxation time of the latter is quite short with respect to the former.

Therefore, $G(t) \sim \exp(-t/\tau_M)$, where τ_M is the Maxwell relaxation time, which is the geometric mean of the relaxation times of both mechanisms.[40] $G(t)$ decaying as a single exponential does not describe the system under study. If $G^*(\omega)$ is calculated for the case where $G(t) \sim \exp(-(t/\tau)^{1/2})$, which corresponds to an intermediate case where the characteristic time, τ, considers reptation and breaking/recombination of the same order of magnitude. Here, the fitting to the experimental data in the Cole–Cole plot is not good as can be observed in Fig. S4 of the ESI.† However, if $G^*(\omega)$ is calculated with $G(t) \sim \exp(-(t/\tau_R)^{1/4})$ that corresponds to the case where stress just relaxes through reptation as in conventional polymers, the fitting to the experimental $G'(\omega)$ and $G''(\omega)$ curves is quite good for several orders of magnitude as observed in Fig. 7b and Fig. S4 of the ESI.† This case corresponds to micelles that do not break and reform, in contrast to Maxwellian fluids; they are completely frozen as in the case of chemically bonded polymers.

3.3 DWS microrheology

Mean square displacements (MSDs). $g^{(2)}(\tau)$ from the scattered light of a DWS experiment due to embedded probe particles (diam. a = 2 μm) can be related to their $\langle \Delta \boldsymbol{r}^2(t) \rangle$ through a numerical algorithm.[24] Fig. 8 presents typical $\langle \Delta \boldsymbol{r}^2(t) \rangle$ *vs.* t curves measured for micellar solutions with different $C_{PBPEO57}$ spanning in time over three orders of magnitude. We observe two different regimes of motion. At short times, there is a regime where $\langle \Delta \boldsymbol{r}^2(t) \rangle$ is essentially a linear function of time consistent with $\langle \Delta \boldsymbol{r}^2(t) \rangle = 6D_0t$, where D_0 is the diffusion coefficient of the microspheres in the solvent at infinite dilution. Our average value is $D_0 = 0.13 \times 10^{-14}$ m^2 s^{-1} which is close to the particle diffusion in pure water $D_0 \sim 0.21 \times 10^{-14}$ m^2 s^{-1}. At intermediate times, $\langle \Delta \boldsymbol{r}^2(t) \rangle$ does not reach a constant value as in other complex fluids where a plateau is observed. In this case, we observe just an inflection point around 0.3 ms, from where motion is subdiffusive. At a time above $t \sim 5$ ms, we were unable to see a plateau, that is, microspheres are never trapped by the micellar network. Here, our MSDs are quite noisy because we were not able to conduct DWS experiments for a very long time since the viscosity of the suspensions was very low, and the microspheres started to sediment; when I^* started to decline, we ended the experiment (10 min for low concentrations −15 min for higher concentrations). Instead of the behavior observed in other WLM solutions, in our case at longer times, we never reached the regime where the MSD is again a linear function of time when particles are released from the trap when the stress relaxed. It is interesting to note that there is a clear difference between the $\langle \Delta \boldsymbol{r}^2(t) \rangle$ curves for WLMs made of PBPEO57 and those made of standard surfactants or PBPEO45 as observed in Fig. 8 and Fig. S5 of the ESI.† There, we include examples of WLM systems made of: (a) PBPEO45 at 1 wt% and 2 wt% (recall that at ∼2.5 wt% a phase transition appears). Here, the curves behave like those of PBPEO57, except that at ∼1 to 2 ms a plateau starts which can be observed where the particles could be trapped in the micellar network; (b) *N*-tetradecyl-*N*,*N*-dimethyl-3-ammonio-1-propanesulfonate (TDPS), sodium dodecyl sulfate (SDS), and salty water.[29] Here, the network is made of WLMs which allows the particles to escape after the stress relaxes through a process of breaking and recombination; therefore, this system follows the Maxwell model at low and intermediate frequencies.[29] (c) Suspensions made of semi-flexible cylinders of fd virus (length ∼ 1 μm).[41] Here, the $\langle \Delta \boldsymbol{r}^2(t) \rangle$ curves measured by DWS are more similar to those of PBPEO57.

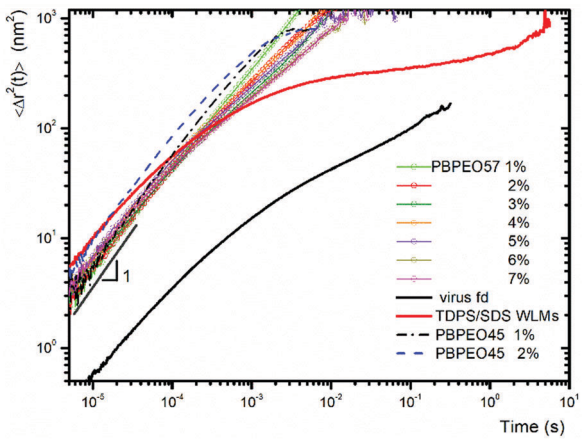

Fig. 8 $\langle \Delta \boldsymbol{r}^2(t) \rangle$ *vs.* t for microspheres in PBPEO57 micellar solutions. For comparison, we include data for micellar solutions of PBPEO45 (1 wt% blue dot-dashed line and 2 wt% black dashed line), suspensions of fd virus (a = 1 μm, C_{fd} = 25 mg ml^{-1} and [NaCl] = 225 mmol L^{-1}, black line), and WLM solutions of TDPS/SDS/brine (C_{TDPS} = 46 mmol L^{-1}, R = 0.45, [NaCl] = 0.5 mol L^{-1}, red line).

Viscoelastic spectra. The $\langle \Delta \boldsymbol{r}^2(t) \rangle$ curves were fitted to the model curve given by Bellour *et al.*,[28] as described in the Experimental section to obtain $G^*(\omega)$ at high frequency, using eqn (1). The numerical fitting parameters in the model do not give any physical insight in this case due to the lack of the mentioned plateau, although the overall fitting was excellent and helped to calculate $G^*(\omega)$ with a small error. In Fig. 9, we present the viscous (imaginary part, Fig. 9a) and elastic (real part, Fig. 9c) components, respectively, of the complex modulus $G^*(\omega)$ for the PBPEO57 micellar solutions at T = 20 °C. In Fig. 9a, the lines correspond to measurements using mechanical rheology, and the squares correspond to the microrheology. For $G''(\omega)$, there is a small tie error between both sets of curves, which is in the range of less than 1 Pa; this is quite reasonable. Fig. 9b presents the whole spectra for $G''(\omega)$ along eight decades in time for $C_{PBPEO57}$ = 4, 5, and 6 wt%. The tie error for $G'(\omega)$ is much larger than for $G''(\omega)$ as observed in Fig. 9c. The microrheological values of $G'(\omega)$ around $\omega \sim 4$ to 6×10^2 s^{-1} present an unexplained change in curvature. Consequently, there is an unexpected faster decay in the frequency region which comes from the highest measured values of $\langle \Delta \boldsymbol{r}^2(t) \rangle$. These time values correspond to the sector where $g^{(2)}(\tau) \sim 0$ and noisy; the numerical error here is large, because it is not clear how the correlation function has to be truncated, and probably this error affects more $G'(\omega)$ than $G''(\omega)$ at these frequencies.

Fig. 10 presents $G'(\omega)$ and $G''(\omega)$ obtained with mechanical rheology (low and intermediate frequencies) and microrheology (high frequencies) for the PBPEO57 micellar system (Fig. 10a); for comparison, we included the system made of PBPEO45 (Fig. 10b).

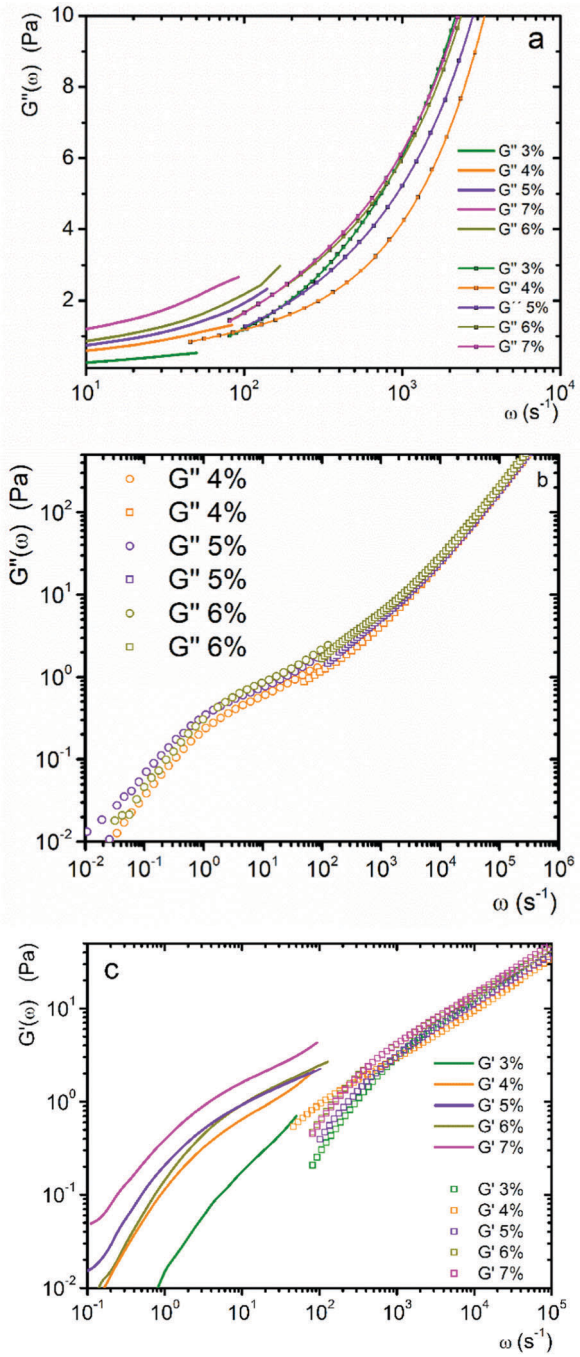

Fig. 9 Shear moduli *vs.* ω from mechanical rheology (lines) and microrheology (symbols). (a) $G''(\omega)$ *vs.* ω. (b) $G''(\omega)$ *vs.* ω in the logarithmic scale along eight decades in frequency for $C_{PBPEO57}$ = 4, 5, and 6 wt%. (c) $G'(\omega)$ *vs.* ω.

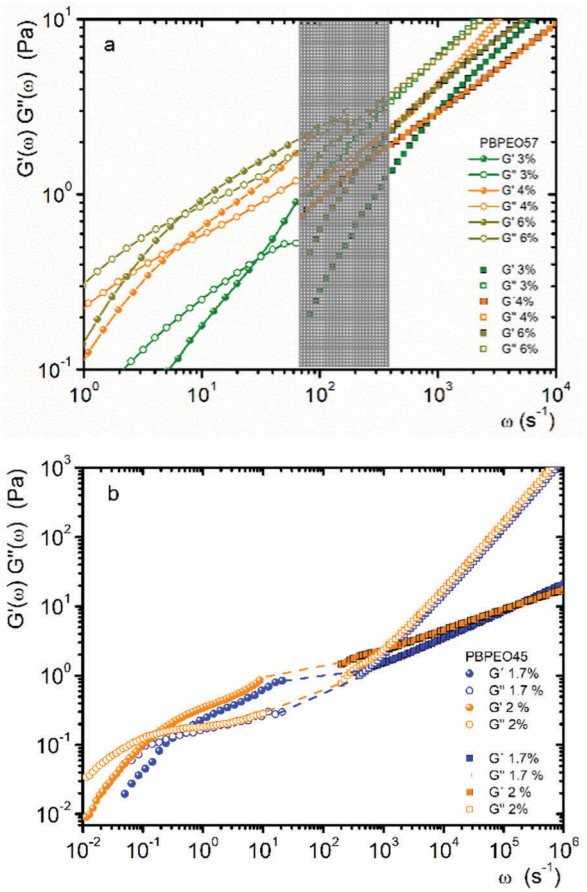

Fig. 10 $G'(\omega)$ and $G''(\omega)$ obtained by rheology and microrheology for both micellar systems: (a) PBPEO57, here we included a gray window where the crossing is expected to be found and where the measured $G'(\omega)$ values are probably not accurate; (b) PBPEO45, microrheology could not reach the mechanical measurements; the gap is represented by dashed lines.

In both cases at high frequency, $G''(\omega)$ is larger than $G'(\omega)$. In contrast, as mentioned above, after the first crossing at ω_0, $G'(\omega) > G''(\omega)$ and before this crossing $G'(\omega) < G''(\omega)$. Therefore, a second crossing point must be observed at some point in the high-frequency range. For PBPEO57, the $G'(\omega)$ and $G''(\omega)$ curves approach each other, but we could not capture the crossing, because $G'(\omega)$ decays faster around $\omega \sim 4$ to 6×10^2 s^{-1}, as mentioned before. Therefore, in Fig. 10a, we included a gray window where the crossing is expected to be found, and we estimate that $G'(\omega)$ values are not accurate. For PBPEO45, the second crossing was captured (Fig. 10b), but the MSD data never reached the long times needed to obtain the lower values of the microrheological moduli necessary to tie with the mechanical measurements. Hence, we have a gap (dashed lines between 10 s^{-1} $\leq \omega \leq$ 120 s^{-1}), although the mechanical measurements seem to be the continuation of the microrheological data.

At high frequencies, micelles can be regarded as semi-flexible chains where the stress relaxation processes, reptation and breaking/recombination, are mostly still. Stress relaxes *via* intramicellar processes as ω increases; first it is dominated by the Rouse–Zimm modes and then by the internal relaxation of individual Kuhn segments. Thus, at high frequencies, $|G^*|$ exhibits a power law behavior, $|G^*| \sim \omega^{\nu}$, illustrated in Fig. 11a and Fig. S6 of the ESI,† with an exponent $\nu \sim 5/9$ in the Rouse–Zimm regime that changes at a critical frequency, ω^*, to $\nu \sim 3/4$, where the internal bending modes of Kuhn segments dominate. This change occurs at the shortest relaxation time in the Rouse–Zimm spectrum. At very high frequencies, $G^*(\omega)$ is dominated by the solvent, that is water, $G^*(\omega) = -i\eta_s\omega$. Using $\omega^* \approx k_BT/8\eta_s l_p^3$,[42,43]

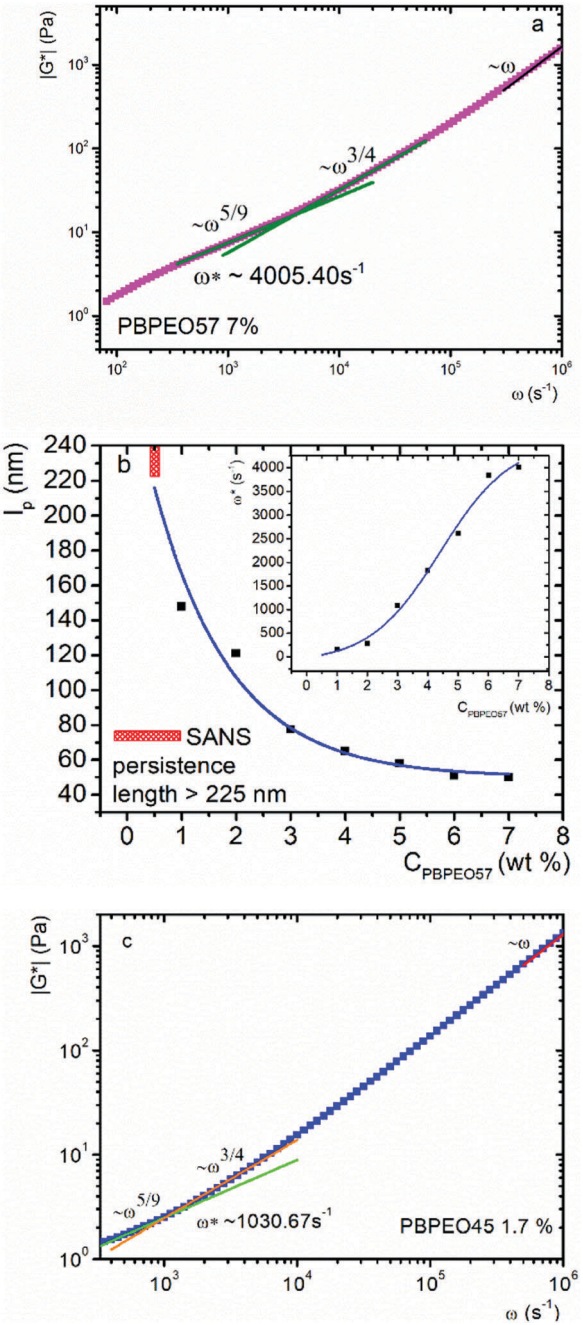

Fig. 11 (a) Power law behavior of $|G^*| \sim \omega^{\nu}$ for PBPEO57 WLMs at high frequencies. First, it is dominated by the Rouse–Zimm modes, then as ω increases by the internal relaxation of individual Kuhn segments, and finally by the viscous water. $C_{PBPEO57}$ = 7 wt%. (b) l_p as a function of concentration for the PBPEO57 WLMs obtained with microrheology. A red dashed square was included for the region where l_p must be found using SANS. Inset: ω^* *vs.* $C_{PBPEO57}$. Blue lines are a guide to the eye. (c) An example of the power law behavior of the PBPEO45 WLMs at high frequencies.

the persistence length of the WLMs is estimated. We found that ω^* depends on concentration as illustrated in the inset of Fig. 11b. In Fig. 11b, we present l_p *vs.* $C_{PBPEO57}$. The interaction between WLMs sensibly modifies l_p, since it increases faster as the concentration decreases close to C^*. In this figure, we also included the area (in red) where the experimental l_p value obtained using SANS should be found at 0.5 wt% (>225 nm). If we extrapolate our concentration-dependent l_p to the concentration where the SANS measurement was done, the agreement is quite reasonable. This behavior of a marked decrease of l_p with concentration increase has been observed in cylindrical polymer brushes in the dilute and semi-dilute regime using SANS[38] and in polyelectrolyte chains.[44,45] The explanation for this fact in these systems also seems to be applied here. In the dilute solution ($<C^*$), the macromolecules adopt a worm-like configuration due to the steric interaction between the side chains, in the case of polymer brushes, or due to the electrostatic repulsion, in polyelectrolyte chains. For both systems, the contribution of the intermolecular interactions to the total free energy increases upon increasing the concentration. To reduce this contribution, a reduction in l_p of the thread-like structures occurs because for a flexible macromolecule the excluded volume that is not available for the other macromolecules is smaller than the corresponding one of a rigid macromolecule.

In Fig. 11c, we included an example of the power law behavior of $|G^*|$ for PBPEO45 WLMs at high frequencies. Here with microrheology, the estimated value of l_p is $\sim$ 76 nm at 1.7 wt% which is slightly above C^*. This value is smaller than that obtained by SANS, $l_p \sim$ 141 nm at 0.5 wt%. Observing how fast is the increase of l_p at low concentrations in the case of the PBPEO57, this value could be reasonable. In this case, we do not have enough points to make a reasonable estimation because the range of concentrations able to be studied is too small (see Fig. S7 of the ESI†).

4. Conclusion

It was found that PBPEO57 in water self-assembles in WLMs with a diameter of ~12.7 nm, a core radius of ~2.7 nm, a shell thickness of ~3.0 nm and an estimated persistence length of >225 nm. The degree of polymerization of PB and PEO blocks is 37 and 57, respectively. We compared this system with another similar system, the PBPEO45 that also forms WLMs in water with the same core as before, but with a PEO block with a degree of polymerization of 45. In the latter, the diameter was ~12.8 nm, the core radius was very similar to that of the PBPEO57 ~2.6 nm and the shell thickness was ~3.1 nm, although with a smaller estimated persistence length of ~141 nm. The bending energy is more significant for the PBPEO57 WLMs than that for the PBPEO45. The stiffness difference is because the PEO block is already more densely packed in the WLMs of PBPEO57 than of PBPEO45, any bending will increase this steric overcrowding.

The micelles of PBPEO57 do not follow the rheological behavior of the WLM solutions of conventional surfactants. At low concentration, the micellar solutions steadily shear-thins as the shear rate increases reaching low viscosity values at large shear rates; there are no shear-thickening peaks. The boundary between dilute and semidilute regimes was estimated according to the behavior of the zero-shear viscosity to be ~0.8 wt%. When sheared, the micellar solutions present

birefringence. The viscoelastic spectra at low and intermediate frequencies do not follow the Maxwell model. The micelles of PBPEO57 do not break and reform. The same behavior was observed in the case of PBPEO45, which also produces an atypical WLM solution. The slow dynamics of the self-assembly explains this uncommon behavior of a WLM system; any micellar rearrangement is impeded due to the extremely high hydrophobicity of the PB block.

The mean square displacement of colloidal particles was measured in the micellar solution of PBPEO57 and compared with other fluids with embedded thread-like structures (conventional surfactant WLMs, fd virus, and PBPEO45 WLMs). From the particle mean square displacement, we obtained $G'(\omega)$ and $G''(\omega)$ at high frequencies. $|G^*|$ exhibits a power law behavior. Here, it is evident where the stress relaxation changes from the Rouse–Zimm modes to the bending modes of Kuhn segments at ω^*. From here, l_p was calculated for the PBPEO57 WLMs, which is concentration dependent, but extrapolating our data to the concentration where the SANS measurement was done, the agreement is reasonable. As concentration increases, a reduction in l_p of the thread-like structures occurs to reduce the contribution of the interaction to the total free energy, because for a flexible macromolecule the excluded volume that is not available for the other macromolecules is smaller than the corresponding one of a rigid macromolecule.

In summary, we obtained information about the relaxation mechanisms of the system at low (mainly through reptation) and high frequencies (Rouse–Zimm and bending modes), and how they are related to the size of the PEO shell and the diblock copolymer concentration.

Disclaimer

Specific commercial equipment, instruments, materials, suppliers, software, *etc.* are identified in this paper to foster understanding. Such identification does not imply recommendation or endorsement by the National Institute of Standards and Technology, nor does it imply that the materials or equipment identified are necessarily the best available for the purpose.

Conflicts of interest

There are no conflicts to declare.

Acknowledgements

Financial support from SEP-CONACyT (Projects: Infraest. 280010, FC 076, and 237425), DGAPA-UNAM (IN 106218), and PRODEP (B. A.-G. postdoctoral fellowship) are gratefully acknowledged. We also thank Dr S. Tehuacanero-Cuapa for his help to get the SEM and TEM images, MSc S. Ramos for his technical help, Dr A. Selmani for her preliminary rheological measurements, and Dr E. Sarmiento-Gomez for his critical discussions.

References

1 *Soft Matter Physics*, ed. M. Daoud and C. E. Williams, Springer Berlin, Heidelberg, 1999.
2 *Soft and Fragile Matter*, ed. M. E. Cates and M. R. Evans, SUSSP publications, 2000.
3 S. J. Holder and N. A. J. M. Sommerdijk, *Polym. Chem.*, 2011, **2**, 1018.
4 I. W. Hamley, *Angew. Chem., Int. Ed.*, 2003, **42**, 1692.
5 T. Gadt, N. S. Leong, G. Cambridge, M. A. Winnik and I. Manners, *Nat. Mater.*, 2009, **8**, 144.
6 J. Schobel, M. Karg, D. Rosenbach, G. Krauss, A. Greiner and H. Schmalz, *Macromolecules*, 2016, **49**, 2761.
7 S. Nehache, P. Tyagi, M. Semsarilar, A. Deratani, T. N. T. Phan, D. Gigmes and D. Quemener, *Soft Matter*, 2017, **13**, 6689.
8 N. Dan and S. A. Safran, *Adv. Colloid Interface Sci.*, 2006, **123-126**, 323.
9 E. B. Zhulina, M. Adam, I. LaRue, S. S. Sheiko and M. Rubinstein, *Macromolecules*, 2005, **38**, 5330.
10 B. Lonetti, A. Tsigkri, P. R. Lang, J. Setllbrink, L. Willner, J. Kohlbrecher and M. P. Lettinga, *Macromolecules*, 2011, **44**, 3583.
11 Y. Y. Won, H. T. Davis and F. S. Bates, *Science*, 1999, **283**, 960.
12 Y. Y. Won, K. Paso, H. T. Davis and F. S. Bates, *J. Phys. Chem. B*, 2001, **105**, 8302.
13 S. Jain and F. S. Bates, *Science*, 2003, **300**, 460.
14 S. Jain and F. S. Bates, *Macromolecules*, 2004, **37**, 1511.
15 S. Jain, X. Gong, L. E. Scriven and F. S. Bates, *Phys. Rev. Lett.*, 2004, **96**, 138304.
16 S. Forster, B. Berton, H. P. Hentze, E. Kramer, M. Antonietti and P. Linder, *Macromolecules*, 2001, **34**, 4610.
17 Y. Y. Won, H. T. Davis, F. S. Bates, M. Agamalian and G. D. Wignall, *J. Phys. Chem. B*, 2000, **104**, 7134.
18 Y. Y. Won, H. T. Davis and F. S. Bates, *Macromolecules*, 2003, **36**, 953.
19 S. Förster, M. Konrad and P. Lindner, *Phys. Rev. Lett.*, 2005, **94**, 17803.
20 B. Lonetti, J. Kohlbrecher, L. Willner, J. K. G. Dhont and M. P. Lettinga, *J. Phys.: Condens. Matter*, 2008, **20**, 404207.
21 B. Arenas-Gomez, M. Vincekovic, C. Garza and R. Castillo, *Eur. Phys. J. E: Soft Matter Biol. Phys.*, 2014, **37**, 51.
22 S. R. Kline, Reduction and Analysis of SANS and USANS Data Using IGOR Pro, *J. Appl. Crystallogr.*, 2006, **39**, 895.
23 T. G. Mason, *Rheol. Acta*, 2000, **39**, 371.
24 J. Galvan-Miyoshi, J. Delgado and R. Castillo, *Eur. Phys. J. E: Soft Matter Biol. Phys.*, 2008, **26**, 369.
25 S. A. Prahl, M. J. C. van Gemert and A. J. Welch, *Appl. Opt.*, 1993, **32**, 559.
26 S. A. Prahl, Inverse Adding Doubling, http://omlc.ogi.edu/software/iad/index.html.
27 E. Sarmiento-Gomez, B. Morales-Cruzado and R. Castillo, *Appl. Opt.*, 2014, **53**, 4675.
28 M. Bellour, M. Skouri, J.-P. Munch and P. Hébraud, *Eur. Phys. J. E: Soft Matter Biol. Phys.*, 2002, **8**, 431.

29 E. Sarmiento-Gomez, D. Lopez-Diaz and R. Castillo, *J. Phys. Chem. B*, 2010, **114**, 12193.
30 S. Asahina, T. Togashi, O. Terasaki, S. Takam, T. Adschiri, M. Shibata and N. Erdman, *Microsc. Anal.*, 2012, **26**, S12.
31 Y. Zhao, A. M. Jamieson, B. G. Olson, N. Yao, S. Dong, S. Nazarenko, X. Hu and J. Lal, *J. Polym. Sci., Part B: Polym. Phys.*, 2006, **44**, 2412.
32 B. Hammouda, *J. Appl. Crystallogr.*, 2010, **43**, 716.
33 C. A. Dreiss, *Soft Matter*, 2007, **3**, 956.
34 A. Guinier and G. Fournet, *Small-Angle Scattering of X-Rays*, Wiley, New York, 1955.
35 J. S. Pedersen and P. Shurtenberger, *Macromolecules*, 1996, **29**, 7602.
36 W. R. Chen, P. D. Butler and L. J. Magid, *Langmuir*, 2006, **22**, 6539.
37 P. Dalhaimer, H. Bermudez and D. E. Discher, *J. Polym. Sci., Part B: Polym. Phys.*, 2004, **42**, 168.
38 S. Bolisetty, S. Rosenfeldt, C. N. Rochette, L. Harnau, P. Lindner, Y. Xu, A. H. E. Müller and M. Ballauff, *Colloid Polym. Sci.*, 2009, **287**, 129.
39 Y. Y. Won, A. K. Brannan, H. T. Davis and F. S. Bates, *J. Phys. Chem. B*, 2002, **106**, 3354.
40 M. E. Cates, *Macromolecules*, 1987, **20**, 2289.
41 E. Sarmiento-Gomez, D. Montalvan-Sorrosa, C. Garza, J. Mas-Oliva and R. Castillo, *Eur. Phys. J. E: Soft Matter Biol. Phys.*, 2012, **35**, 35.
42 F. Gittes and F. C. MacKintosh, *Phys. Rev. E: Stat. Phys., Plasmas, Fluids, Relat. Interdiscip. Top.*, 1998, **58**, 1241.
43 N. Willenbacher, C. Oelschlaeger, M. Schopferer, P. Fischer, F. Cardinaux and F. Scheffold, *Phys. Rev. Lett.*, 2007, **99**, 68302.
44 M. J. Stevens and K. Kremer, *Phys. Rev. Lett.*, 1993, **71**, 2228.
45 A. Yethiraj, *Phys. Rev. Lett.*, 1997, **78**, 3789.
46 J. S. Pedersen, *Adv. Colloid Interface Sci.*, 1997, **70**, 171.

